ACS Applied Materials and Interfaces 12.11 (2020): 12500-12509

DOI: https://doi.org/10.1021/acsami.9b22827

10-Fold Quantum Yield Improvement of Ag_2S Nanoparticles by Fine Compositional Tuning

Alicia Ortega-Rodríguez[2,6], Yingli Shen[1,3], Irene Zabala Gutierrez[2] , Harrison David Santos[1,3], Vivian Torres Vera[2], Erving Ximendes[1,3], Gonzalo Villaverde[2], José Lifante[1,3] Christoph Gerke[2], Nuria Fernández[1,3], Oscar G. Calderón[4], Sonia Melle[4], José Marques-Hueso[5], Diego Mendez-Gonzalez[2], Marco Laurenti[1,2], Callum M.S. Jones[5], Juan Manuel López-Romero[6], Rafael Contreras-Cáceres[2], Daniel Jaque[1,3]*, Jorge Rubio-Retama[1,2]**

1 Nanobiology Group, Instituto Ramón y Cajal de Investigación Sanitaria, IRYCIS Madrid, 28034, Spain
2 Departamento de Química en Ciencias Farmacéuticas, Universidad Complutense de Madrid, 28040, Spain.
3 Fluorescence Imaging Group, Facultad de Ciencias, Universidad Autónoma de Madrid, Madrid 28049, Spain.
4 Departamento de Óptica, Universidad Complutense de Madrid, 28037 Madrid, Spain
5 Institute of Sensors, Signals and Systems (ISSS), School of Engineering & Physical Sciences (EPS), Heriot-Watt University, Edinburgh, EH15 2BR, United Kingdom
6 Departamento Química Orgánica, Facultad de Ciencias, Universidad de Málaga, Málaga, 29071, Spain

E-mail: bjrubio@ucm.es,

Keywords: Ag_2S/Ag nanoparticles, fluorescent probes, Synthesis optimization, PL lifetime, PLQY, NIR-II imaging.

Abstract

Ag_2S semiconductor nanoparticles are near-infrared luminescent probes with outstanding properties (good biocompatibility, optimum spectral operation range, and easy biofunctionalization) that make them ideal probes for *in vivo* imaging. Ag_2S nanoparticles have, indeed, made possible amazing challenges including *in vivo* brain imaging and advanced diagnosis of cardiovascular system. Despite the continuous redesign of synthesis routes, the emission quantum yield (QY) of Ag_2S nanoparticles is typically below 0.2%. This leads to a low luminescent brightness that avoids their translation into the clinics. In this work, an innovative synthetic methodology that permits a 10-fold increment in the absolute quantum yield from 0.2% up to 2.3% is presented. Such an increment in the QY is accompanied by an enlargement of photoluminescence (PL) lifetimes from 184 ns to 1200 ns. The optimized synthetic route here presented here is based on a fine control over both the Ag core and the Ag/S ratio within the nanoparticles. Such control reduces the density of structural defects and decreases non-radiative pathways. In addition, we demonstrate that the superior performance of the Ag_2S nanoparticles allows for high contrast *in vivo* bioimaging.

1. Introduction

Biomedical imaging techniques are used routinely in clinical practice as they provide physiological information of organs/tissues of living beings that is, otherwise, unreachable.[1, 2] These non-invasive techniques allow the diagnose and/or prognosis of different diseases and have gained increasing interest in clinical and medical research. Among them, computed tomography (CT), positron emission tomography (PET) or single-photon emission tomography (SPECT), magnetic resonance imaging (MRI), ultrasonography (Echo) and optical coherent tomography (OCT) are by far the most used ones. However, some drawbacks such as the use of ionizing radiation (CT, PET, and SPECT), limited spatial resolution (MRI, Echo and PET), poor temporal resolution (CT, MRI, PET and SPECT) and complex and expensive instrumentation restrict their access to third-level hospitals[3, 4].

Some of these drawbacks are overcome by near-infrared (NIR) fluorescent imaging in the so-called second NIR window which is ranged between 1000 and 1700 nm and it is characterized by a reduction of the scattering and absorption of tissues.[5, 6] *In vivo* imaging in this spectral range has been widely demonstrated to provide better imaging resolution at larger depths into tissues.[7] The simplicity of the instrumentation as well as the high spatial and temporal resolution have facilitated, for instance, its use in medical research where animal models are used to study the localization and the evolution of diseases, thus facilitating a successful translation from research to clinical practice.[8, 9] However, apart from being biocompatible, one of the major challenges to widen its application is related to the low quantum yield (QY) of most of the NIR fluorescent probes. For instance, Dai's group has reported organic compounds that emit in the NIR-II region which can be used as fluorescent NIR-II probes[10]. Among them CH1055, a conjugated organic molecule with good biological features has shown a QY=0.4%[11], while other organic compounds, like cholate functionalized single wall carbon nanotubes (SWNT), have shown a relative QY= 0.84%.[12] Inorganic nanoparticles based on heavy metal ions like PbS or CdHgTe have excellent fluorescent properties in the NIR-II region with QY about 40%[13, 14], however, these classes of nanoparticles have been discarded due to their known acute and chronic toxicity.[15,16]

Silver chalcogenides can be considered as promising alternative candidates for NIR-II fluorescent imaging due to its negligible toxicity and high photostability.[17-19] However, their low luminescence brightness is still a big obstacle that limits their application for high contrast, deep tissue *in vivo* imaging. Many works dealing with Ag_2S nanoparticles obtain QY as high as 10%,[20, 21] however, most of these results are obtained by comparison with NIR-II fluorescent dyes that do not match with absolute QYs measured with an integrating sphere and which are

typically below 1%.[22] This low QY agree with short PL lifetimes observed in these nanoparticles, ranging between 50 ns and 200 ns, that reveals the dominant role of non-radiative pathways within the emission process.[23, 24] These non-radiative processes are associated with the presence of certain regions on the nanoparticle's surface that act as charge acceptors, dissociating excitons and therefore reducing the photoluminescence efficiency.[25] Some of these traps are related to variations in solvent or surface-bound coordinating ligands (dangling bonds) that influence the steady-state, time-resolved photoluminescence and QY.[26] In addition, structural defects in the crystalline structure can also strongly affect the photoluminescence efficiency of the nanoparticles since they induce the formation of midgap states that favor non-photoluminescence pathways and reduce the photoluminescence efficiency of the nanoparticles.[27] Furthermore, in the case of Ag_2S nanoparticles, the high redox potential of silver ions and the high temperature used during their synthesis can lead to the formation of a metallic silver core when the reaction is carried out in the presence of amines, forming Ag^+-amine complexes which are highly reactive and can form Ag_2S as well as Ag nanoparticles.[28,29] To minimize the formation of the metallic silver core, different authors have proposed to remove, totally or partially, the presence of amine bearing molecules and use dodecanethiol instead, thereby reducing the reactivity and passivate the surface of the nanoparticles.[30] However the resulting nanoparticles still presented low QY[31] as well as short PL lifetimes[32, 33]. In this work, we have developed a new synthesis route towards the improvement of the fluorescence properties of Ag_2S nanoparticles. A systematic study of the steady-state luminescence, emission lifetime and absolute QYs of nanoparticles with different metallic silver contents demonstrate that the presence of a specific amount of metallic silver within the nanoparticles increases by more than one order of magnitude the QY of the nanoparticles. This increment is concomitant with an enlargement of the PL lifetime which scales from 180 ns to 1220 ns as well as an emission redshift of the produced Ag_2S/Ag nanoparticles. The potential use of the improved Ag_2S nanoparticles for high contrast *in vivo* imaging in the second biological window has been also evaluated.

2. Experimental Section

2.1. Chemicals

Silver nitrate (99%), sodium diethyldithiocarbamate (NaDDTC) (ACS reagent grade), oleylamine (70%) (OLA), 1-dodecanethiol (≤98%) (DDT), 11-mercaptoundecanoic acid (95%) (MUA), $CHCl_3$ (99,6%), ethanol (99.9%), *N*-(3-(dimethylamino)propyl)-*N*′-ethylcarbodiimide hydrochloride (EDC) (99%), *N*-hydroxysulfosuccinimide sodium salt (Sulfo-NHS) (98%), *O*-

(2-aminoethyl)-*O'*-methyl- polyethylene glycol (PEG-NH_2, M_p = 5.000 g/mol), and PBS tablets were purchased from Sigma-Aldrich and used as received. Commercial Ag_2S-PEG nanoparticles were bought from NIR Optics technology.

2.2. Characterization

Transmission electron microscopy (TEM) studies were carried out using a TEM Talos F200X operated at 80 kV. Zeta-potential experiments were carried out using a Malvern Nano-ZS. The FTIR spectra were obtained using a Nicolet IR200 FTIR spectrometer. X-ray diffraction patterns were recorded on a Philips X'pert diffractometer (Cu-Kα radiation, 45 kV, 40 mA). Data were collected from 2θ = 20–90° with a step size of 0.02° and a normalized count time of 1 s/step. The emission spectra upon illuminating the samples with an 800 nm CW laser were collected with an Andor iDus InGaAs 491 cooled to -90ºC. The absolute photoluminescence QY was measured with a calibrated spectrofluorometer (Edinburgh Instruments, FLS920) equipped with an integrating sphere (Jobin-Yvon). A Xe lamp has been used as excitation source, filtered with a long-pass filter (610 nm) and a monochromator (wavelength: 800 nm, bandwidth: 20 nm). Luminescence was detected by a liquid nitrogen cooled NIR photo-multiplier tube (Hamamatsu, R5509-72). The QY has been calculated by dividing the total number of emitted photons in the 900-1700 nm range by the total number of absorbed photons at 800 nm. Luminescence decay curves were obtained by exciting the colloidal suspensions of nanoparticles by an OPO oscillator (Lotis) tuned to 800 nm, which provides 8 ns pulses at a repetition rate of 10 Hz. Fluorescence intensity was detected with a Peltier cooled photomultiplier tube with enhanced sensitivity in the NIR-II (Hamamatsu R5509-73). The contribution of scattered laser radiation was removed by using two band-pass filters (FEL850 from Thorlabs) as well as a high brightness monochromator (Shamrock 320 from Andor). The time evolution of the fluorescence signal was finally recorded and averaged by a digital oscilloscope (LeCroyWaverunner 6000).

High-angle annular dark field (HAADF) scanning TEM and EDX mappings were conducted by using a FEI Talos F200X (FEI, USA) coupled to a EDX detector. Samples for TEM were prepared by adding 10 μL of each dispersion on a Cu grid with a carbon support membrane, followed by drying.

2.3. *in vivo* imaging

NIR-II *in vivo* images were obtained in a homemade NIR-II system. A fiber-coupled diode laser operating at 800 nm was used as excitation source (LIMO30-F200-DL808). The illumination intensity was controlled via adjustment of diode current. An anesthetized mouse was placed on

a homemade temperature-controlled plate operating at 36 ºC. The NIR-II fluorescence image was acquired with a Peltier cooled InGaAs camera (Xeva 320 from Xenics). The InGaAs detector was cooled down to -40 ºC. Two long-pass filters (FEL850 from Thorlabs) were used to remove the background signal generated by the scattered laser radiation.

in vivo experiments were approved by the regional authority for animal experimentation of Comunidad de Madrid and were conducted in agreement with the Universidad Autónoma de Madrid (UAM) Ethics Committee, in compliance with the European Union directives 63/2010UE and Spanish regulation RD 53/2013. For this study, a total of 15 CD1 female mice (8-14 weeks old, weighing 25-39 g) bred at the animal facility at UAM were used. Mice were anesthetized prior to the imaging experiments in an induction chamber with a continuous flow of 4% isoflurane (Forane, AbbVie Spain, S.L.U) in 100% oxygen until loss of righting reflex was confirmed and breathing rhythm was significantly slowed. Anesthesia was maintained throughout the experiments by means of facemask inhalation of 1.5% isoflurane and core body temperature was kept at 36 ± 1 °C, as measured with a rectal probe, using a heating pad.

2.4. Synthesis of the Ag_2S/Ag-PEG nanoparticles

The synthesis of the Ag_2S/Ag-PEG nanoparticles was carried out in different steps as explained below.

2.4.1. Synthesis of Ag_2S/Ag nanoparticles

The production of the Ag_2S/Ag nanoparticles was carried out as follows: a given amount of Ag(DDTC) typically 25 mg (0.1 mmol) was added into a two-necked round bottom flask at room temperature, which contained 5 mL of a solvent mixture based on OLA and DDT. Table S1 shows the solvent mole fraction (χ_{DDT}) used in each synthesis, where $\chi_{DDT} = (n_{DDT}/(n_{DDT} + n_{OLA}))$. Once all the reagents were introduced within the flask, the mixture was submitted to vacuum for 10 min to remove air and then filled with N_2. After that, the mixture was heated to 190ºC under magnetic stirring with a heating rate of 20ºC/min and under slow magnetic stirring. The reaction was kept for 1 hour and subsequently cooled down naturally. The synthesized nanoparticles were collected by addition of ethanol, which reduces the colloidal stability of the nanoparticles. To do that, 10 mL of ethanol were added to the raw product and centrifuged at 10,000 rpm for 10 min, this process was repeated twice. Finally, the as-prepared product was dispersed in 10 mL of chloroform and stored for further steps.

2.4.2. PEGylation of Ag_2S/Ag heterodimers

With the aim of providing hydrophilicity to the synthesized nanoparticles, they were treated with MUA. This molecule can displace the hydrophobic ligands on the nanoparticles' surface and introduce carboxylic groups on the surface of the nanoparticles, thereby providing good colloidal stability in water. With that purpose, 20 mg (0.1 mmol) of MUA was added to a 1 mL dispersion containing 1 mg/mL of Ag_2S/Ag nanoparticles in chloroform at room temperature. After that, the mixture was sonicated in an ultrasonic bath for 10 minutes until the Ag_2S/Ag nanoparticles lost their colloidal stability and precipitated at the bottom of the flask. Then, the precipitate was collected and dispersed in 1 mL of PBS at pH 7.4. Subsequently, these nanoparticles were covered with PEG-NH_2 (M_p = 5000 g/mol) via EDC/NHS coupling. To do that, 0.5 mg of EDC and 0.7 mg of sulfo-NHS were dissolved in 1 mL of PBS containing 1 mg of the previously prepared Ag_2S/Ag presenting MUA ligands and 1 mg of PEG-NH_2. The mixture was gently stirred for 2 hours and after this time the nanoparticles were collected by centrifugation at 12.000 rpm for 2 hours. This process was repeated three times and the resulting nanoparticles were dispersed in 1 mL of PBS and stored at 4ºC.

3. Results and discussion

Figure 1 depicts HAADF-STEM images of the Ag_2S nanoparticles synthesized using different solvent ratios. As observed, all the nanoparticles exhibit two well-differentiated regions, a white area with higher Z-contrast, corresponding to the electrodense parts of the nanoparticles, probably due to the presence of metallic Ag into the nanoparticle. In addition, the figure shows the existence of less electrodense areas that appear as grey regions, corresponding to Ag_2S.

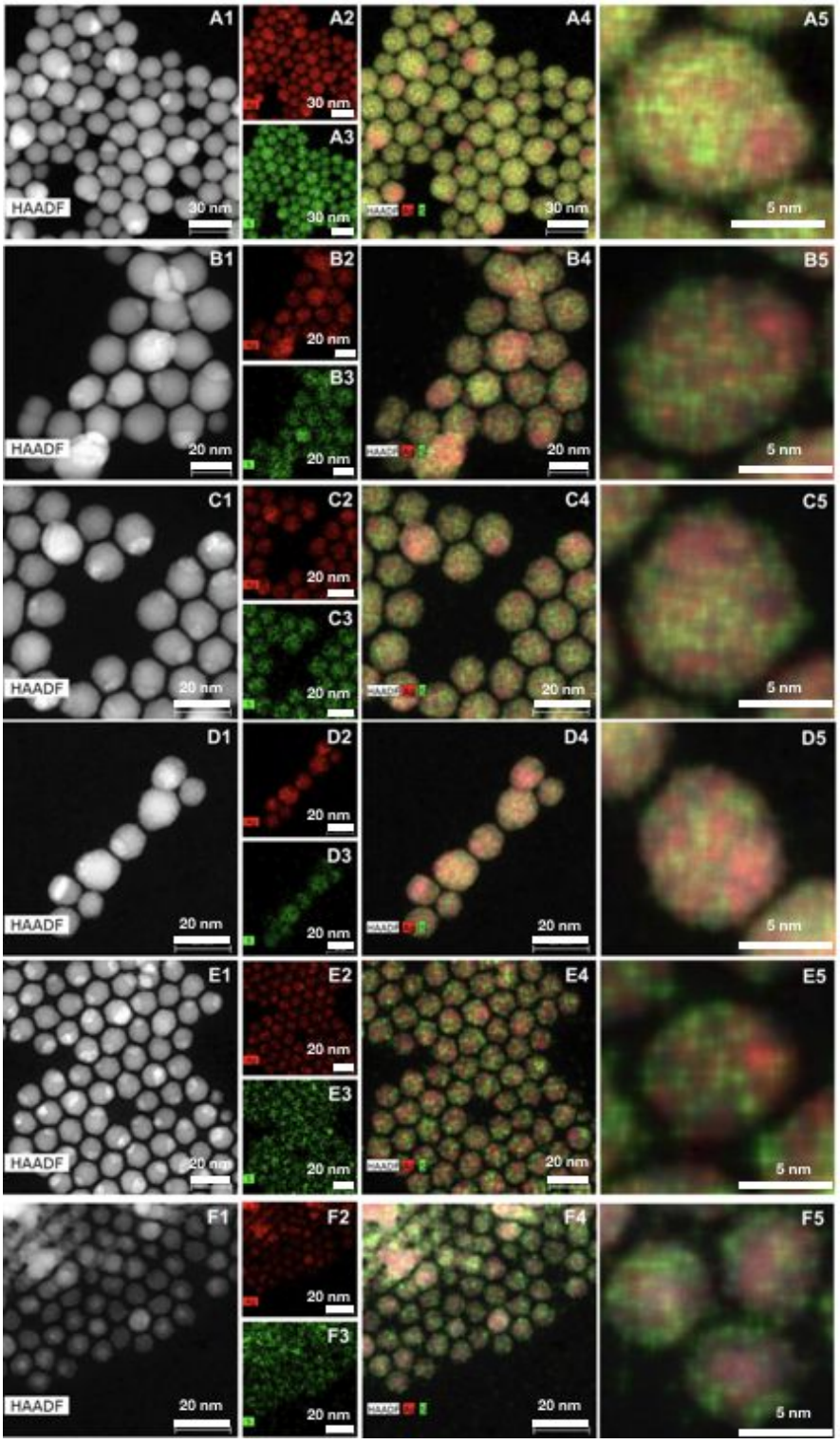

Figure 1. HAADF-STEM micrograph of nanoparticles obtained under different synthetic conditions (from A1 to F1). The insets from A2 to F2 represent the EDS elemental mapping of silver while the insets from A3 to F3 depict the EDS elemental mapping of sulfur. From A4 to F4, merged figures resulting from the HAADF-STEM and EDS elemental analysis are showed. The insets from A5 to F5 show detailed magnifications of the merged EDS and HAADF-STEM micrographs.

The EDS elemental mappings showed in Figure 1 reveal the anisotropic spatial distribution of Ag (red) and S (green) within the nanoparticles. These micrographs unveil the presence of Ag enriched regions that overlap with those that exhibited higher Z-contrast (white regions in the HAADF-STEM). Interestingly, this silver core appears more eccentrically located when lower χ_{DDT} is used during the synthesis. The synthetic conditions induce variations in the structure and properties of the synthesized nanoparticles. In fact, a decrease in overall nanoparticle size can be clearly correlated to an increase of χ_{DDT} during the reaction . **Figure S2** shows the average size of each synthesis as well as the size of the electrodense region that corresponds to the silver core. This result can be explained in terms of the higher capacity of the DDT molecules to interact with the nanoparticles through the thiol group, which exhibits the highest binding energy towards noble metals (200 kJ/mol).[34] Therefore, a high χ_{DDT} (high amount of DDT) leads to an increased colloidal stability of small nanoparticles formed during the course of the reaction and thus preventing the particles from aggregation resulting in a smaller overall nanoparticle size.

XRD patterns of these nanoparticles reveal the presence of two crystalline phases, which could be attributed to monoclinic Ag_2S (JCPDS card No. 14-0072; lattice constants: a = 4.229 Å, b = 6.931 Å, c = 7.862 Å) and cubic Ag (JCPDS card No. 04-0783; lattice constants: a = 4.0862 Å), as seen in **Figure S3**. A more detailed analysis of the XRD can be found in the supporting information. With the aim of completing the structural and compositional characterization XPS and XANE analysis have been carried out. Wide scan survey spectra of the NPs show the presence of Ag 3d (364 eV, 374 eV) and S 2p (161 eV, 162.2 eV) doublets as well as C 1s (285 eV), O 1s (532 eV). High-resolution scans of Ag 3d spectra are shown in Figure S4A. The deconvolution of the Ag 3d binding energy spectra are fitted with two silver doublets. The Ag^+ binding energy of the peaks centred at 372.2 eV (3d3/2) and 366.6 eV(3d5/2) could be attributed with the Ag_2S, whereas those peaks at 373.6 eV (3d3/2) and 367.5 eV (3d5/2) could be related with Ag0, see Figure S4B. Complementary analyses carried out by X-ray absorption near edge structure (XANES) for the Ag K-edge spectra of the synthesized NPs have been also carried out. This technique permit determining the oxidation state of the Ag atoms that constitute the sample. The oxidation state of the samples was analyzed by linear combination fitting procedure as seen in Figure S6. The result of these analyses shows that in both cases the NPs are constituted by a predominant phase of Ag_2S and a metallic Ag counterpart in a ratio 0.75:1. Furthermore, we have performed Fourier transform EXAFS of

both types of NPs as seen in Figure S7. As one can observe, both samples (Ag2S-0 and Ag2S-06) exhibit two main peaks, one located at 2 Å, which matches perfectly with the Ag-S distance in Ag_2S phase and a second peak at 2.8 Å, which is characteristic of Ag-Ag distance in metallic Ag phase and we can conclude that the synthesized Ag_2S NPs have a metallic Ag phase within the structure.

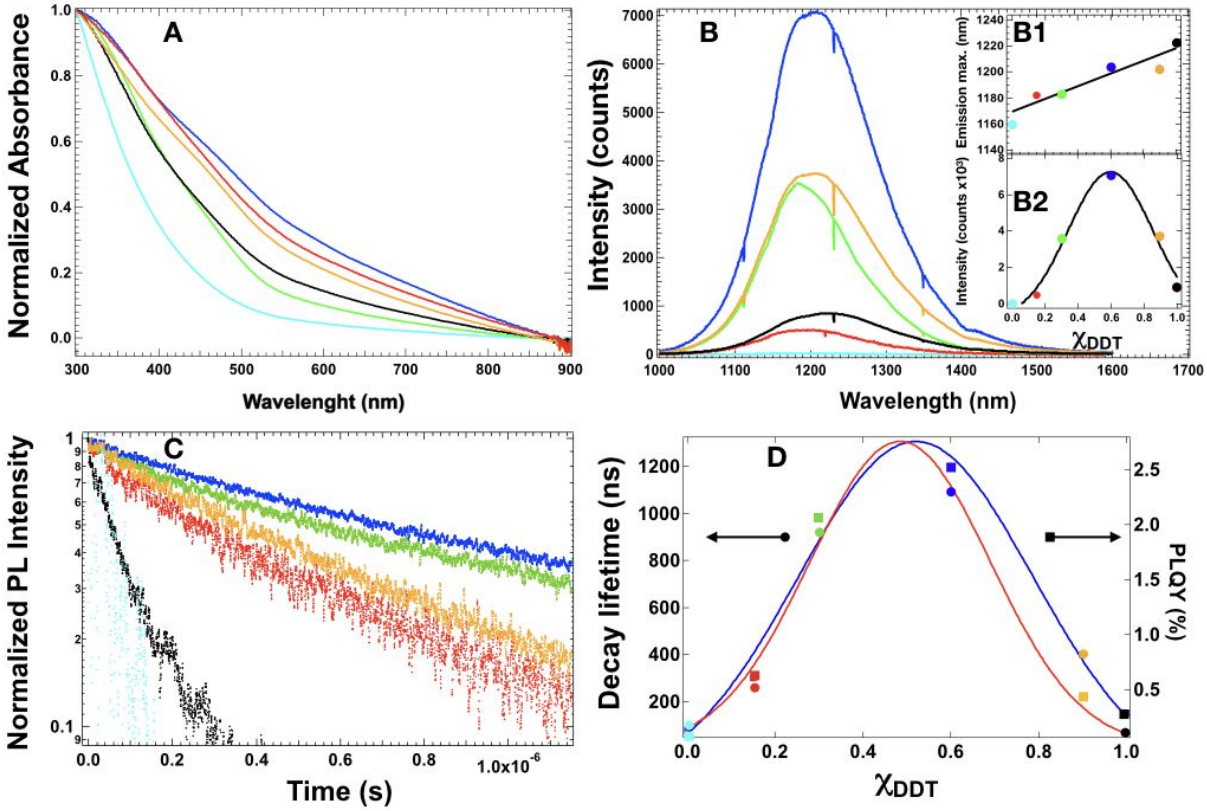

Figure 2. A) Normalized UV-Vis spectra of the nanoparticles synthesized under different solvents ratios. B) PL spectra of the NPs synthesized under different conditions dispersed in CHCl3 at a concentration of 1 mg/mL. (exc. 800 nm). Insets B1 and B2 show the variation of the maximum of the emission wavelength and the maximum of the PL intensity as a function of the solvent ratio. C) PL decay curves of the different nanoparticles. D) Lifetimes and absolute quantum yields as a function of the solvent ratio. The color legend is as follows: Ag_2S-0.00 cyan, Ag_2S-0.15 red, Ag_2S-0.30 green, Ag_2S-0.60 blue, Ag_2S-0.90 orange, Ag_2S-1.00 black, with numeric values indicating the χ_{DDT}.

Figure 2 summarizes the impact of the synthetic conditions on the spectroscopic properties of the nanoparticles (absorption, photoluminescence, lifetime and QY). **Figure 2A** shows the

normalized absorption spectra for all samples in the range between 300 to 900 nm. In all cases, a strong absorption in the visible region with weak shoulder at 465 nm and a long tail until the NIR region can be observed. The shoulder at ~465 nm may be attributed to the plasmonic contribution of the metallic Ag present in the nanoparticle.[35,36] It is important to note that this band only appears in those syntheses in which OLA is used. This indicates the role of the amino groups in the formation of metallic silver during the synthesis of the nanoparticles at high temperatures.[33] In fact, it is well known that the synthesis of Ag_2S nanoparticles through the thermal decomposition of a silver precursor, like Ag-monothiobenzoate or Ag-diethyldithiocarbamate, metallic Ag nanocrystals are formed as side products.[37,38] This is because the dissociation energy of the Ag-S bond (206.45 kJ/mol) is lower compared to that of the S-C bond (265.95 kJ/mol) and, under a heating-up process, Ag ions are released in the absence of reactive sulfur.[39] The addition of alkylamines in the reaction may lower the dissociation energy of the S-C bonds of the silver precursor via nucleophilic addition of an amine to the carbonyl group, thereby potentially providing a higher amount of reactive sulfur in the reaction resulting in an increased Ag_2S formation.[40] Such an effect can be observed in **Figure S1**, here one can observe the reduction of the size of the Ag_2S matrix when increasing χ_{DDT}, whilst the size of the Ag core remains unchanged.

Figure 2B shows the emission band of the different samples as obtained under 800 nm optical excitation. The emission band is clearly affected by the synthesis conditions. Firstly, we observe that the peak wavelength is red-shifted when increasing χ_{DDT}. In fact, the nanoparticles synthesized only in the presence of OLA exhibit its maximum emission at 1160 nm, whilst those synthesized using only DDT as solvent showed its emission peak at 1220 nm. These variations indicate an increment in the bandgap of the nanoparticles when increasing the χ_{DDT}, which cannot be attributed to quantum confinement effects, since the size of all these nanoparticles are well above the Bohr radius of the Ag_2S.[41, 42] Another effect observed is a prominent variation of the luminescence emission intensity as a χ_{DDT}, which could be related to different emission efficiencies. For a better understanding, luminescence decay times of the nanoparticles were measured, see **Figure 2C**. From these results, we can observe an enhancement of the nanoparticle lifetimes from 120 ns to 1200 ns when increasing χ_{DDT} up to 0.60, see **Figure 2D**. Such an increment of the lifetimes is concomitant with the enhancement of the QY that increases from 0.2% to 2.3%. Surprisingly, a further increase of χ_{DDT} provoked a subsequent reduction of the lifetimes from 1200 ns to 180 ns as well as the QY values, from 2.4% down to 0.2%. For the lowest and the highest χ_{DDT} values, decreased PL lifetimes and

QYs could be attributed to the increment of non-radiative pathways in the nanoparticles. All these results allowed us to identify the optimal synthetic conditions for the production of highly efficient Ag_2S nanoparticles.

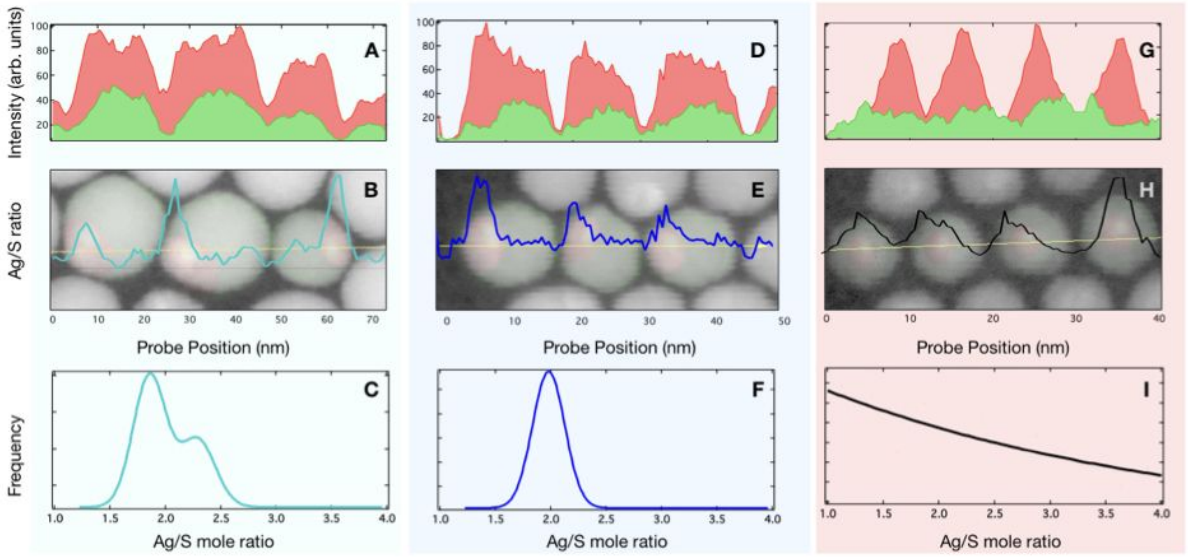

Figure 3. EDS-mapping profile of the Ag_2S/Ag nanoparticles (A, D and G. Net X-ray profile extracted from the yellow arrow marked in the STEM images (B, E, and H). Merged STEM and nanoparticles model images represented as a function of Ag/S ratio versus the probe position (B, E and H). Frequency distribution of the Ag/S ratio in the nanoparticles excluding the silver core (C, F and I). The nanoparticles used for EDS-mapping were derived using χ_{DDT} of 0.00 (A-B), 0.60 (D-F) and 1.00 (G-I) during synthesis.

In order to understand how synthetic conditions could affect the emission of the nanoparticles, we have analyzed the composition of the generated nanoparticles by EDS-mapping profile as seen in **Figure 3**. It is evidenced how the synthetic conditions affect tremendously the size, the shape, the position of the Ag enriched core and also the atomic ratio of Ag/S within the nanoparticles. In fact, the analysis of the Net X-ray profile of those nanoparticles synthesized with neat OLA (χ_{DDT} of 0.00, **Figure 3A**) allows to infer the Ag/S atomic ratio profile of such nanoparticles as seen in **Figure 3B** that is characterized by the presence of peaks that match with the position of the silver enriched region, while the rest of the regions present Ag/S atomic ratios around 2. When we represent the frequency distribution of the Ag/S ratio obtained in

these nanoparticles, we can observe the presence of two Gaussian populations, one cantered at 1.8 and other at 2.2, which differs from a theoretical ratio of 2, which should correspond to a perfect Ag_2S matrix (**Figure 3C)**. Such a result would indicate the presence of compositional inhomogeneities in the Ag_2S matrix that could render in structural defects. This fact would explain the low QY observed in this sample.[43] Interestingly, those nanoparticles synthesized using a χ_{DDT} of 0.60 depict and Net X-ray profile different than the previous nanoparticles, see **Figure 3D**. That informs us of Ag/S ratios very close to 2 for those areas distinct to the silver enriched regions, as seen in **Figure 3G**. When we represent the frequency distribution of the Ag/S ratio, we obtain a mean value centered at 1.9, which is closer to the hypothetical ratio of 2 the Ag_2S matrix and would indicate the reduction of possible defects as shown in **Figure 3F**. That would be the reason why these nanoparticles exhibit an increment of the static emission as well as the PL lifetime and QY. Finally, in the case of those nanoparticles synthesized in the presence of neat DDT (χ_{DDT} of 1.00), the Net X-ray profile shows the presence of a high concentration of silver, located preferentially in the core of the nanoparticles, **Figure 3G**. Such a profile creates a rapid increment of the Ag/S atomic ratio from a S enriched surface to a Ag enriched core, giving as a result a very small region where the matrix composition could be Ag_2S, decreasing the NIR fluorescence of these nanoparticles, as shown in **Figure 3H**. On the contrary, the frequency distribution of the Ag/S ratio does not permit us to observe any maximum close to 2, which would indicate the presence of a thin Ag_2S region surrounded by structural defects, which would render Ag_2S nanoparticles with poor luminescent properties as observed in **Figure 3I**.

The optimized (from synthesis with χ_{DDT} of 0.60 with largest QY and luminescence lifetime) Ag_2S nanoparticles were tested as NIR-II *in vivo* imaging contrast agents. To do that, ligand exchange reaction is carried out to substitute the hydrophobic capping agents by hydrophilic, thiol bearing molecules for their stabilization in aqueous media. **Figure 4A** shows the ligand exchange process. In the first step, carboxylic acid terminated MUA ligands are introduced on the nanoparticles' surface, thereby acquiring negative charges which is confirmed by Zeta-potential measurements giving a value of ~ -27 mV. The hydrodynamic diameter of the MUA-functionalized nanoparticles is 14± 7 nm in PBS. After that, carboxylic groups were used as anchoring points, allowing for the linkage of PEG-NH_2 molecules (5 kDa) through the amino terminated group, performing a coupling reaction mediated by EDC and sulfo-NHS. The products of this reaction are PEG-modified nanoparticles with a hydrodynamic diameter of 20 ± 9 nm and a Zeta-potential of -16 mV, which is still negative due to the presence of remaining

carboxylate groups on the surface of the nanoparticles that did not react with PEG, as seen in **Figure 4**. After the ligand exchange reaction, the luminescence lifetime decreased as evident in **Figure 4C**, when these nanoparticles were coated with PEG and transfer to PBS, the lifetime suffered a reduction from 1200 ns down to 379 ns. The observed reduction of the lifetime can be associated to the environment assisted multiphoton relaxation processes, when the nanoparticles are dispersed in water, as it was previously observed.[24] For the shake of comparison, we also measured the luminescence decay time of commercially available Ag_2S-PEG nanoparticles in PBS (see **Figure 4C**). Note that our "optimized" Ag_2S nanoparticles showed a significantly increased luminescence decay time, revealing the effective reduction of non-radiative decays due to the improved Ag and S ratio in the final matrix.

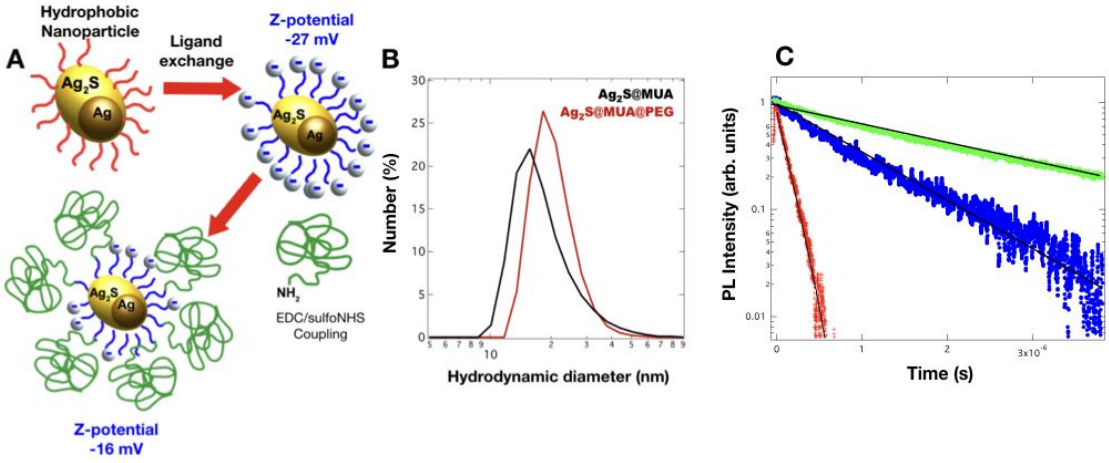

Figure 4. A) Schematic representation for the surface modification of the nanoparticles by ligand exchange reaction with MUA and its subsequent PEGylation through EDC/sulfo-NHS coupling reaction. Graphic B) Evolution of the nanoparticle hydrodynamic diameter during the surface functionalization process. C) PL decay times of Ag_2S/Ag nanoparticles in $CHCl_3$ (green), Ag_2S/Ag-PEG nanoparticles in PBS at a concentration of 1 mg/mL (blue) and Ag_2S-PEG nanoparticles synthesized by Zhang's method in PBS at a concentration of 1.5 mg/mL (red).

In order to demonstrate the potential of the "optimized" Ag_2S nanoparticles for *in vivo* imaging, 150 µL of a solution with a nanoparticle concentration of 1 mg/mL were injected in 1 month-old CD1 female mice via retro-orbital injection. The anesthetized mouse was illuminated with a low power 800 nm laser diode providing an on-target laser power density as low as 45 mW/cm^2. The luminescence generated by the Ag_2S nanoparticles was registered by an InGaAs

infrared camera. In order to avoid any contribution of laser reflected light to the fluorescence image, a 1000 nm long-pass filter was used. In **Figure 5A**, an optical+infrared fluorescence merged image of the mouse, as obtained 5 minutes after the injection of the nanoparticles, is shown. A clear luminescence signal is detected at the abdominal area of the mouse which is attributed to a fast accumulation of nanoparticles in the liver. Although the highest intensity is detected from the liver, a detailed inspection of the sub-abdominal region reveals also clear fluorescence contrast. The zoom included in **Figure 5B** reveals the presence of nanoparticles in the bloodstream. In particular, vessels of the lower limbs are evident in the amplified fluorescence image. Indeed, it is clear that, even by using this low excitation power density and low magnification optics, the optimized Ag_2S nanoparticles are bright enough to provide an image of the vessel anatomy with a sub-millimeter spatial resolution (see intensity profile in **Figure 5C**). In order to elucidate the biodistribution of the injected nanoparticles, the animal was sacrificed 1 hour after injection and the presence of Ag_2S in the different organs was elucidated from their fluorescence images. **Figure 5D** shows the fluorescence image corresponding to the skeleton, indicating the partial accumulation of Ag_2S nanoparticles within bones. **Figure 5E** includes the infrared fluorescence images corresponding to the liver, spleen, and lungs. Only these organs provided any relevant infrared fluorescence. This fact indicates that 1 hour post-injection the Ag_2S nanoparticles were accumulated at bones, lungs, liver, and spleen. Similar biodistribution patterns were already reported by other authors[44, 45]. Finally, **Figure 5F** shows an amplified fluorescence image of the bone structure of a limb. Note how the accumulation of Ag_2S nanoparticles at bones opens the way of obtaining high-resolution images of the skeleton by infrared fluorescence imaging. At this point we would like to stress that the accumulation of Ag_2S nanoparticles at bone structures could not only be used for advanced in vivo imaging of bone structure but it can be also used for therapeutic effects. Note that Ag_2S nanoparticles, are also known to be excellent luminescent nanothermometers. This means that they could be potentially used to measure intra-bone temperature. This, in turns, becomes essential to achieve full control over photothermal therapies of bones, tat have been recently demonstrated to be of high efficacy to promote bone regeneration.[46,47, 48]

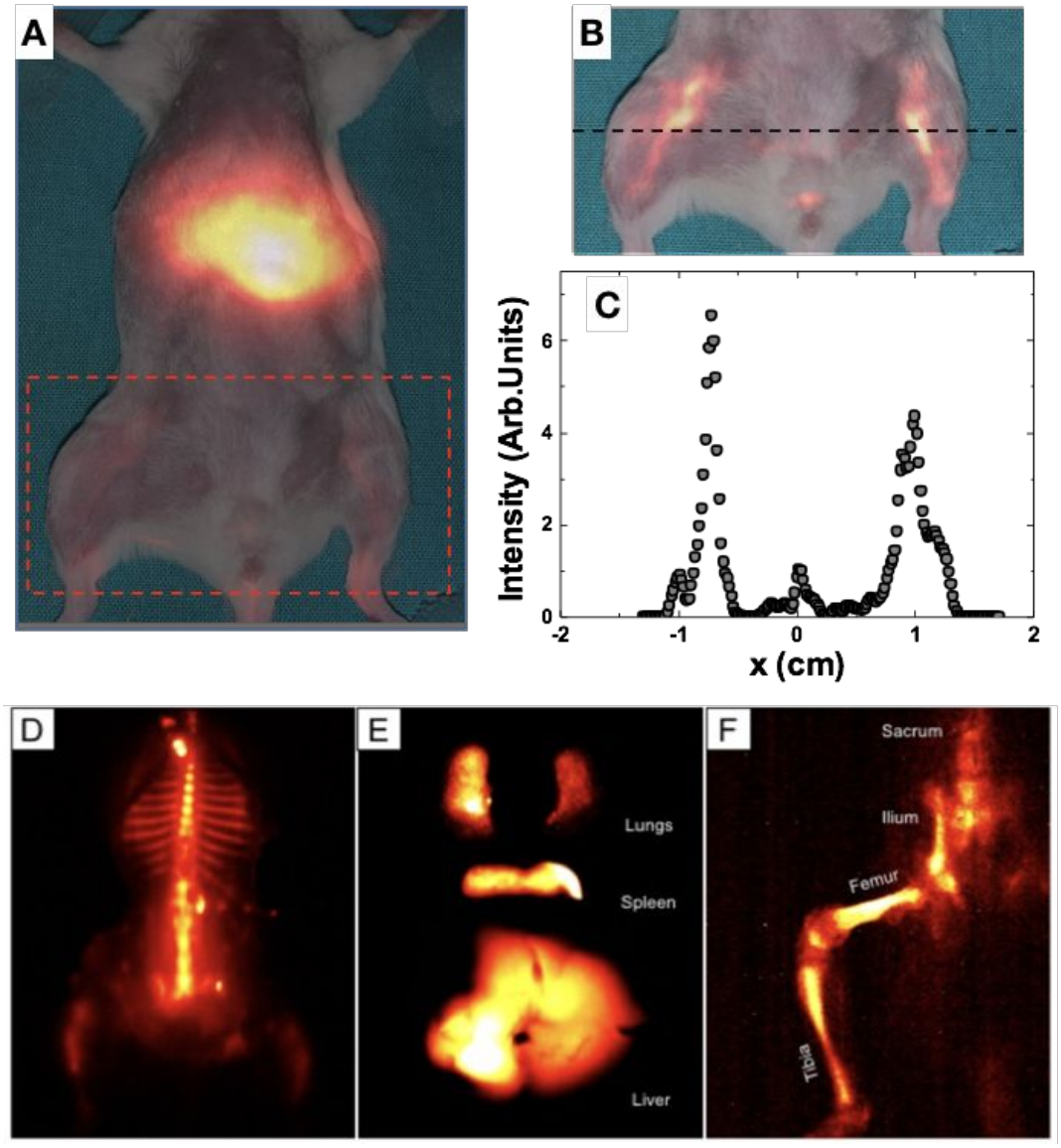

Figure 5. A) *In vivo* imaging of an anesthetized mouse 5 min after intravenous injection of the here optimized Ag_2S nanoparticles. The animal was optically excited with an 800 nm laser diode with a power density of 45 mW/cm^2 and luminescence (1000-1400 nm) was recorded with an infrared camera. B) Magnification of the lower extremities where the femoral vessels can be observed. C) A cross-sectional intensity profile measured along the black dashed line in (B). D) *ex vivo* NIR-II image of dissected mouse of the skeleton E) lung spleen and liver and F) detailed image of femur, tibia, ilium, and sacrum of mice.

4. Conclusions

The present work demonstrates the crucial role of the synthetic conditions on the photoluminescence properties of Ag_2S nanoparticles. More in detail, the effect of the solvent ratio of DDT and OLA during the nanoparticle generation via thermal degradation using an

Ag(DDTC) was evaluated. In total, six different solvent ratios were tested (χ_{DDT} of 0.00, 0.15, 0.30, 0.60, 0.90 and 1.00). From a structural point of view, a clear decrease in nanoparticle size with an increase of DDT was observed, assumingly correlated to a more pronounced stabilization of small nanoparticles by the thiol bearing solvent DDT. Regarding the photoluminescent properties, a maximum of luminescence lifetimes and QY were observed for nanoparticles generated with a χ_{DDT} of 0.60. Measured luminescence lifetimes reached values of 1200 ns in comparison to lifetimes of 120 and 180 ns for the nanoparticles synthesized using χ_{DDT} of 0.00 and 1.00, respectively. For the QY, a 10-fold higher value of 2.3 % was determined for the nanoparticles synthesized with χ_{DDT} of 0.60 compared to the nanoparticles derived from neat solvents. As studied by EDS-mapping of the generated nanoparticles using χ_{DDT} of 0.00, 0.60 and 1.00, we were able to clearly correlate the improved photoluminescent properties to a more precise ratio of Ag and S in the final nanoparticle matrix. In addition, the surface modification of the Ag_2S nanoparticles allows for a transfer into aqueous solution. In this media our fabricated Ag_2S nanoparticles conserve the superb optical properties, exhibiting higher luminescence lifetimes and QY compared to commercially available PEGylated Ag_2S in aqueous buffer. This permits their usage as contrast imaging agents, where the nanoparticles present an excellent biodistribution.

Acknowledgements

This work was partially supported by the Ministerio de Economía y Competitividad de España MAT2017-83111R, MAT2016-75362-C3-1-R, RTI2018-094859-B-100, CTQ2016-76311 by the Comunidad Autónoma de Madrid (B2017/BMD-3867RENIM-CM), and co-financed by the European Structural and investment fund. Additional funding was provided by the European Commission, Horizon 2020 project NanoTBTech. RCC acknowledges fundings to the Comunidad de Madrid for the "Atracción de Talento" fellowship with reference 2018-T1/IND-10736. D.M.G. thanks UCM-Santander for a postdoctoral contract (CT17/17- CT18/17). V.T.V thanks COLFUTURO for a predoctoral scholarship. Authors would like to thank Adolfo Martinez-Orellana for the STEM as well as the elemental mapping analysis.

References

1. Qin, M. Y.; Yang, X. Q.; Wang, K.; Zhang, X. S.; Song, J. T.; Yao, M. H.; Yan, D. M.; Liu, B.; Zhao, Y. D., In vivo cancer targeting and fluorescence-CT dual-mode imaging with nanoprobes based on silver sulfide quantum dots and iodinated oil. *Nanoscale* **2015,** *7* (46), 19484-92.

2. Key, J.; Leary, J. F., Nanoparticles for multimodal in vivo imaging in nanomedicine. *Int J Nanomedicine* **2014,** *9*, 711-26.

3. Chen, Z. Y.; Wang, Y. X.; Lin, Y.; Zhang, J. S.; Yang, F.; Zhou, Q. L.; Liao, Y. Y., Advance of molecular imaging technology and targeted imaging agent in imaging and therapy. *Biomed Res Int* **2014**, 819324, 1-12.

4. Wang, X.; Pang, Y.; Ku, G.; Xie, X.; Stoica, G.; Wang, L. V., Noninvasive laser-induced photoacoustic tomography for structural and functional in vivo imaging of the brain. *Nature Biotech.* **2003,** *21*, 803-806.

5. Hong, G.; Antaris, A. L.; Dai, H., Near-infrared fluorophores for biomedical imaging. *Nature Biomedical Engineering* **2017,** *1* (10), 1-22.

6. Frangioni, J. V., In vivo near-infrared fluorescence imaging. *Curr Opin Chem Biol* **2003,** *7* (5), 626-34.

7. Zhao, J.; Zhong, D.; Zhou, S., NIR-I-to-NIR-II fluorescent nanomaterials for biomedical imaging and cancer therapy. *Journal of Materials Chemistry B* **2018,** *6* (3), 349-365.

8. Hu, F.; Li, C.; Zhang, Y.; Wang, M.; Wu, D.; Wang, Q., Real-time in vivo visualization of tumor therapy by a near-infrared-II Ag2S quantum dot-based theranostic nanoplatform. *Nano Research* **2015,** *8* (5), 1637-1647.

9. Ortgies, D. H.; García-Villalón, Á. L.; Granado, M.; Amor, S.; Rodríguez, E. M.; Santos, H. D. A.; Yao, J.; Rubio-Retama, J.; Jaque, D., Infrared fluorescence imaging of infarcted hearts with Ag2S nanodots. *Nano Research* **2019,** *12* (4), 749-757.

10. Diao, S.; Blackburn, J. L.; Hong, G.; Antaris, A. L.; Chang, J.; Wu, J. Z.; Zhang, B.; Cheng, K.; Kuo, C. J.; Dai, H., Fluorescence Imaging In Vivo at Wavelengths beyond 1500 nm. *Angew Chem Int Ed Engl* **2015,** *54* (49), 14758-62.

11. Antaris, A. L.; Chen, H.; Cheng, K.; Sun, Y.; Hong, G.; Qu, C.; Diao, S.; Deng, Z.; Hu, X.; Zhang, B.; Zhang, X.; Yaghi, O. K.; Alamparambil, Z. R.; Hong, X.; Cheng, Z.; Dai, H., A small-molecule dye for NIR-II imaging. *Nat Mater* **2016,** *15* (2), 235-42.

12. Welsher, K.; Liu, Z.; Sherlock, S. P.; Robinson, J. T.; Chen, Z.; Daranciang, D.; Dai, H., A route to brightly fluorescent carbon nanotubes for near-infrared imaging in mice. *Nat Nanotechnol* **2009,** *4* (11), 773-80.

13. Fernee, M. J.; Thomsen, E.; Jensen, P.; Rubinsztein-Dunlop, H., Highly efficient luminescence from a hybrid state found in strongly quantum confined PbS nanocrystals. *Nanotechnology* **2006,** *17* (4), 956-62.

14. Greben, M.; Fucikova, A.; Valenta, J., Photoluminescence quantum yield of PbS nanocrystals in colloidal suspensions. *Journal of Applied Physics* **2015,** *11,* 144306, 1-7.

15. Rzigalinski, B. A.; Strobl, J. S., Cadmium-containing nanoparticles: perspectives on pharmacology and toxicology of quantum dots. *Toxicol Appl Pharmacol* **2009,** *238* (3), 280-8.

16. Liu, W.; Zhang, S.; Wang, L.; Qu, C.; Zhang, C.; Hong, L.; Yuan, L.; Huang, Z.; Wang, Z.; Liu, S.; Jiang, G., CdSe quantum dot (QD)-induced morphological and functional impairments to liver in mice. *PLoS One* **2011,** *6* (9), e24406, 1-9.

17. Hong, G.; Robinson, J. T.; Zhang, Y.; Diao, S.; Antaris, A. L.; Wang, Q.; Dai, H., In vivo fluorescence imaging with Ag2S quantum dots in the second near-infrared region. *Angew Chem Int Ed Engl* **2012,** *51* (39), 9818-21.

18. Dong, B.; Li, C.; Chen, G.; Zhang, Y.; Zhang, Y.; Deng, M.; Wang, Q., Facile Synthesis of Highly Photoluminescent Ag2Se Quantum Dots as a New Fluorescent Probe in the Second Near-Infrared Window for in Vivo Imaging. *Chemistry of Materials* **2013,** *25* (12), 2503-2509.

19. Liu, Y.-W.; Ko, D.-K.; Oh, S. J.; Gordon, T. R.; Doan-Nguyen, V.; Paik, T.; Kang, Y.; Ye, X.; Jin, L.; Kagan, C. R.; Murray, C. B., Near-Infrared Absorption of Monodisperse Silver Telluride (Ag2Te) Nanocrystals and Photoconductive Response of Their Self-Assembled Superlattices. *Chemistry of Materials* **2011,** *23* (21), 4657-4659.

20. Shen, Y.; Lifante, J.; Ximendes, E.; Santos, H. D. A.; Ruiz, D.; Juarez, B. H.; Zabala Gutierrez, I.; Torres Vera, V.; Rubio Retama, J.; Martin Rodriguez, E.; Ortgies, D. H.; Jaque, D.; Benayas, A.; Del Rosal, B., Perspectives for Ag2S NIR-II nanoparticles in biomedicine: from imaging to multifunctionality. *Nanoscale* **2019,** *11* (41), 19251-19264.

21. Lu, F.; Gong, Y.; Ju, W.; Cheng, F.; Zhang, K.; Wang, Q.; Wang, W.; Zhong, J.; Fan, Q.; Huang, W., Facile one-pot synthesis of monodispersed NIR-II emissive silver sulfide quantum dots. *Inorganic Chemistry Communications* **2019,** *106*, 233-239.

22. Ruiz, D.; Mizrahi, M.; Santos, H. D. A.; Jaque, D.; Jones, C. M. S.; Marques-Hueso, J.; Jacinto, C.; Requejo, F. G.; Torres-Pardo, A.; Gonzalez-Calbet, J. M.; Juarez, B. H.,

Synthesis and characterization of Ag2S and Ag2S/Ag2(S,Se) NIR nanocrystals. *Nanoscale* **2019,** *11* (18), 9194-9200.

23. Jiang, P.; Tian, Z.-Q.; Zhu, C.-N.; Zhang, Z.-L.; Pang, D.-W., Emission-Tunable Near-Infrared Ag2S Quantum Dots. *Chemistry of Materials* **2011,** *24* (1), 3-5.

24. Santos, H. D.; Ruiz, D.; Lifante, G.; Jacinto, C.; Juarez, B. H.; Jaque, D., Time resolved spectroscopy of infrared emitting Ag2S nanocrystals for subcutaneous thermometry. *Nanoscale* **2017,** *9* (7), 2505-2513.

25. Zhang, Y.; Liu, Y.; Li, C.; Chen, X.; Wang, Q., Controlled Synthesis of Ag2S Quantum Dots and Experimental Determination of the Exciton Bohr Radius. *The Journal of Physical Chemistry C* **2014,** *118* (9), 4918-4923.

26. Giansante, C.; Infante, I., Surface Traps in Colloidal Quantum Dots: A Combined Experimental and Theoretical Perspective. *J Phys Chem Lett* **2017,** *8* (20), 5209-5215.

27. Boles, M. A.; Ling, D.; Hyeon, T.; Talapin, D. V., Erratum: The surface science of nanocrystals. *Nat Mater* **2016,** *15* (3),141-153.

28. Doh, H.; Hwang, S.; Kim, S., Size-Tunable Synthesis of Nearly Monodisperse Ag2S Nanoparticles and Size-Dependent Fate of the Crystal Structures upon Cation Exchange to AgInS2 Nanoparticles. *Chemistry of Materials* **2016,** *28* (22), 8123-8127.

29. Ruiz, D.; del Rosal, B.; Acebrón, M.; Palencia, C.; Sun, C.; Cabanillas-González, J.; López-Haro, M.; Hungría, A. B.; Jaque, D.; Juarez, B. H., Ag/Ag2S Nanocrystals for High Sensitivity Near-Infrared Luminescence Nanothermometry. *Advanced Functional Materials* **2017,** *27*, 1604629, 1-9.

30. Sadovnikov, S. I.; Kuznetsova, Y. V.; Rempel, A. A., Ag 2 S silver sulfide nanoparticles and colloidal solutions: Synthesis and properties. *Nano-Structures & Nano-Objects* **2016,** *7*, 81-91.

31. Yan Zhang, G. H., Yejun Zhang, Guangcun Chen, Feng Li, Hongjie Dai, Qiangbin Wang, Ag2S Quantum Dot: A Bright and Biocompatible Fluorescent Nanoprobe in the Second Near-Infrared Window. *ACS Nano* **2012,** *6* (5), 3695-3702.

32. He, H.; Lin, Y.; Tian, Z. Q.; Zhu, D. L.; Zhang, Z. L.; Pang, D. W., Ultrasmall Pb:Ag2 S Quantum Dots with Uniform Particle Size and Bright Tunable Fluorescence in the NIR-II Window. *Small* **2018,** *14* (11), 1703296, 1-7.

33. Liu, W.; Zhang, J.; Peng, Z.; Yang, X.; Li, L.; Chen, Q.; Liu, J.; Wang, K., Controlled formation of Ag2S/Ag Janus nanoparticles using alkylamine as reductant surfactants. *Colloids and Surfaces A: Physicochemical and Engineering Aspects* **2018,** *544*, 111-117.

34. Love, J. C.; Estroff, L. A.; Kriebel, J. K.; Nuzzo, R. G.; Whitesides, G. M., Self-Assembled Monolayers of Thiolates on Metals as a Form of Nanotechnology. *Chem. Rev.* **2004,** *105*, 4, 1103-1170.

35. Mogensen, K. B.; Kneipp, K., Size-Dependent Shifts of Plasmon Resonance in Silver Nanoparticle Films Using Controlled Dissolution: Monitoring the Onset of Surface Screening Effects. *The Journal of Physical Chemistry C* **2014,** *118* (48), 28075-28083.

36. Serrano-Montes, A. B.; Jimenez de Aberasturi, D.; Langer, J.; Giner-Casares, J. J.; Scarabelli, L.; Herrero, A.; Liz-Marzan, L. M., A General Method for Solvent Exchange of Plasmonic Nanoparticles and Self-Assembly into SERS-Active Monolayers. *Langmuir* **2015,** *31* (33), 9205-13.

37. Qun Tang, S. M. Y., Hyun Jin Yang, Yoonmi Lee, Hyun Jae Song, Hye Ryung Byon, and Hee Cheul Choi., Selective degradation of Chemical Bonds: from Single-Source Molecular Precursor to Metallic Ag and Semiconducting Ag2S Nanocrystals via Instant Thermal Activation. *Langmuir* **1996,** *12* (22), 2802-2805.

38. Yaping Du, B. X., Tao Fu, Miao Cai, Feng Li, Yan Zhang, and Qiangbin Wang, Near-Infrared Photoluminescent Ag2S Quantum Dots from a Single Source Precursor. *JACS* **2010,** *132* (5), 1470-1471.

39. Tang, S. M. Y., Hyun Jin Yang, Yoonmi Lee, Hyun Jae Song, Hye Ryung Byon, and Hee Cheul Choi, Selective Degradation of Chemical Bonds: from Single-Source Molecular Precursors to Metallic Ag and Semiconducting Ag2S Nanocrystals via Instant Thermal Activation. *Langmuir* **2006,** *22*, 2802-2805.

40. Lim, W. P.; Zhang, Z.; Low, H. Y.; Chin, W. S., Preparation of Ag(2)S nanocrystals of predictable shape and size. *Angew Chem Int Ed Engl* **2004,** *43* (42), 5685-9.

41. Lin, S.; Feng, Y.; Wen, X.; Zhang, P.; Woo, S.; Shrestha, S.; Conibeer, G.; Huang, S., Theoretical and Experimental Investigation of the Electronic Structure and Quantum Confinement of Wet-Chemistry Synthesized Ag2S Nanocrystals. *The Journal of Physical Chemistry C* **2014,** *119* (1), 867-872.

42. Kashida, S., Electronic structure of Ag2S, band calculation and photoelectron spectroscopy. *Solid State Ionics* **2003,** *158* (1-2), 167-175.

43. Wang, Z.; Gu, T.; Kadohira, T.; Tada, T.; Watanabe, S., Migration of Ag in low-temperature Ag2S from first principles. *J Chem Phys* **2008,** *128* (1), 014704.

44. Jiang, P.; Zhu, C. N.; Zhang, Z. L.; Tian, Z. Q.; Pang, D. W., Water-soluble Ag(2)S quantum dots for near-infrared fluorescence imaging in vivo. *Biomaterials* **2012,** *33* (20), 5130-5.

45. Zhang, Y.; Zhang, Y.; Hong, G.; He, W.; Zhou, K.; Yang, K.; Li, F.; Chen, G.; Liu, Z.; Dai, H.; Wang, Q., Biodistribution, pharmacokinetics and toxicology of Ag2S near-infrared quantum dots in mice. *Biomaterials* **2013,** *34* (14), 3639-46.

46. Yanagi, T.; Kajiya, H.; Kawaguchi, M.; Kido, H.; Fukushima, T., Photothermal stress triggered by near infrared-irradiated carbon nanotubes promotes bone deposition in rat calvarial defects. *J Biomater Appl* **2015,** *29* (8), 1109-18.

47. Heo, D. N.; Ko, W.-K.; Bae, M. S.; Lee, J. B.; Lee, D.-W.; Byun, W.; Lee, C. H.; Kim, E.-C.; Jung, B.-Y.; Kwon, I. K., Enhanced bone regeneration with a gold nanoparticle–hydrogel complex. *J. Mater. Chem. B* **2014,** *2* (11), 1584-1593.

48. Wang, Y.; Hu, X.; Zhang, L.; Zhu, C.; Wang, J.; Li, Y.; Wang, Y.; Wang, C.; Zhang, Y.; Yuan, Q., Bioinspired extracellular vesicles embedded with black phosphorus for molecular recognition-guided biomineralization. *Nat Commun* **2019,** *10* (1), 2829-39.

TOC